

Anion-Rectifying Polymeric Single Lithium-Ion Conductors

Seok-Kyu Cho, Kyeong-Seok Oh, Jong Chan Shin, Ji Eun Lee, Kyung Min Lee, Junbeom Cho, Won Bo Lee, Sang Kyu Kwak,* Minjae Lee,* and Sang-Young Lee*

Polymeric single lithium (Li)-ion conductors (SICs), along with inorganic conducting materials such as sulfides and oxides, have received significant attention as promising solid-state electrolytes. Yet their practical applications have been plagued predominantly by sluggish ion transport. Here, a new class of quasi-solid-state SICs based on anion-rectifying semi-interpenetrating polymer networks (semi-IPNs) with reticulated ion nanochannels are demonstrated. This semi-IPN SIC (denoted as sSIC) features a bicontinuous and nanophase-separated linear cationic polyurethane (cPU), which supports single-ion conducting nanochannels, and ultraviolet-crosslinked triacrylate polymer, which serves as a mechanical framework. The cPU phase is preferentially swollen with a liquid electrolyte and subsequently allows anion-rectifying capability and nanofluidic transport via surface charge, which enable fast Li^+ migration through ion nanochannels. Such facile Li^+ conduction is further enhanced by tuning ion-pair (i.e., freely movable anions and cations tethered to the cPU chains) interaction. Notably, the resulting sSIC provides high Li^+ conductivity that exceeds those of commercial carbonate liquid electrolytes. This unusual single-ion conduction behavior of the sSIC suppresses anion-triggered interfacial side reactions with Li-metal anodes and facilitates electrochemical reaction kinetics at electrodes, eventually improving rate performance and cycling retention of Li-metal cells (comprising $\text{LiNi}_{0.8}\text{Co}_{0.1}\text{Mn}_{0.1}\text{O}_2$ cathodes and Li-metal anodes) compared to those based on carbonate liquid electrolytes.

batteries, electrolytes play a key role in determining overall electrochemical reactions. Commercial lithium (Li)-ion batteries typically use liquid electrolytes due to their well-balanced electrochemical attributes and interfacial stability with electrodes that are based on the rocking-chair operation principle.^[4,5]

Meanwhile, stimulated by the rapidly increasing demand for high energy density batteries, Li-metal batteries (i.e., Li-metal anodes coupled with high-capacity cathodes) have recently garnered considerable attention as a promising candidate to outperform Li-ion batteries.^[3,6] Yet the performances of Li-metal batteries currently suffer from poor electrochemical compatibility with liquid electrolytes. Specifically, counter anions and solvents of the liquid electrolytes tend to cause undesirable interfacial side reactions with the Li-metal anodes, resulting in low Coulombic efficiency, dendritic Li growth, and the formation of a passivation layer.^[7,8] The interfacial instability of the liquid electrolytes with Li-metal anodes remains a formidable obstacle in developing Li-metal batteries for practical applications.

1. Introduction

The rapidly approaching era of smart and ubiquitous energy will involve the widespread uses of electric vehicles, wearable and flexible electronics, intelligent robots, and grid-scale energy storage. Anticipation of this energy future has spurred the development of advanced rechargeable batteries with high energy density and safety.^[1–3] Among the core components of

Of the many research efforts undertaken to resolve this challenge, solid-state single-ion conductors (SICs) that allow selective Li^+ migration have been extensively investigated,^[9,10] in addition to synthesis and engineering of new liquid electrolytes.^[11,12] Previous studies on SICs mostly focused on inorganic solid electrolytes such as sulfides and oxides.^[10,13–17] Yet their use in Li-metal batteries remains elusive due to several unresolved problems pertaining to grain-boundary and interfacial

S.-K. Cho, K.-S. Oh, S.-Y. Lee
Department of Chemical and Biomolecular Engineering
Yonsei University
50 Yonsei-ro, Seodaemun-gu, Seoul 03722, Republic of Korea
E-mail: syleek@yonsei.ac.kr

J. C. Shin, M. Lee
Department of Chemistry
Kunsan National University
558 Daehak-ro, Gunsan, Jeollabuk-do 54150, Republic of Korea
E-mail: minjae@kunsan.ac.kr

J. E. Lee, K. M. Lee, S. K. Kwak
School of Energy and Chemical Engineering
Ulsan National Institute of Science and Technology (UNIST)
50 UNIST-gil Eonyang-eup, Ulsan-gun, Ulsan 44919, Republic of Korea
E-mail: skkwak@unist.ac.kr

J. Cho, W. B. Lee
School of Chemical and Biological Engineering
Institute of Chemical Processes
Seoul National University
1 Gwanak-ro, Gwanak-gu, Seoul 08826, Republic of Korea

 The ORCID identification number(s) for the author(s) of this article can be found under <https://doi.org/10.1002/adfm.202107753>.

DOI: 10.1002/adfm.202107753

resistances, hygroscopicity, mechanical rigidity, and complex cell fabrication. Besides inorganic SICs, polymeric SICs are explored due to their mechanical flexibility and intimate interfacial contact with electrodes.^[18–23] However, polymeric SICs contain anionic moieties that are covalently tethered to polymer backbones and typically form strong intermolecular electrostatic interactions with free Li⁺ ions, which eventually hampers Li⁺ conduction.^[24–27] This sluggish Li⁺ transport of polymeric SICs poses a critical problem that has, so far, hindered their widespread application in Li-metal batteries.

Here, we address the aforementioned challenges of SICs by developing a new class of quasi-solid-state SICs based on anion-rectifying semi-interpenetrating polymer networks (semi-IPNs) with reticulated ion nanochannels, which supports accelerated Li⁺ transport that can outperform those of commercial carbonate liquid electrolytes. This semi-IPN SIC (referred to as sSIC) comprises a bicontinuous nanophase-separated linear cationic polyurethane (cPU) and ultraviolet (UV)-crosslinked ethoxylated trimethylolpropane triacrylate (ETPTA) polymer. The cPU phase is preferentially swollen with liquid electrolytes to allow single Li⁺ transport through ion nanochannels, while the UV-crosslinked ETPTA phase that hardly contains liquid electrolyte serves as a mechanical framework. Notably, the cPU phase is designed to provide anion-rectifying (i.e., anion-trapping) capability. In other words, counter anions that originate from the liquid electrolyte are electrostatically captured by the cationic nanochannel walls of the cPU phase. Moreover, the cPU phase accelerates Li⁺ migration by surface charge-governed nanofluidic transport phenomena. Single Li⁺ conduction through the cPU phase is further enhanced by tuning ion-pair (freely movable anions in liquid electrolytes and cations covalently tethered to cPU chains) interactions. As a result, the sSIC provides higher Li⁺ conductivity (namely, ion conductivity multiplied by Li⁺ transference number (t_{Li^+})) and lower activation energy (E_a) for ion conduction compared to those of commercial carbonate liquid electrolytes.

The feasibility of sSICs for practical use is investigated by integrating the sSIC into a Li-metal cell (comprising LiNi_{0.8}Co_{0.1}Mn_{0.1}O₂ (NCM811) cathode and Li-metal anode). Notably, the sSIC, driven by its unusual single Li⁺ conduction behavior, suppresses anion-triggered interfacial side reactions with Li-metal anodes and facilitates the electrochemical reaction kinetics at electrodes, which ultimately improves the rate performance and cycling retention compared to those of a control cell containing a commercial carbonate liquid electrolyte. Moreover, the sSIC demonstrates potential for applications in anode-free cells.

2. Results and Discussion

cPUs with various counter anions were synthesized via the polycondensation reaction of dihydroxy pyrrolidinium salts and methylene diphenyl diisocyanate (MDI) in dimethyl sulfoxide (DMSO, solvent) (Figure 1a). The chemical structures of the as-synthesized cPUs were interrogated by using analyzing nuclear magnetic resonance (NMR) spectra (Figure S1, Supporting Information). Details of the synthesis of the cPU are described in the Experimental method. Among the cPU samples synthesized herein,

the cPU with the bulkiest anion (BPh₄[−]) was selected by considering the effect of anions on the electrochemical properties of sSIC, the details of which will be discussed in the following section.

The sSIC was prepared by using a UV curing-assisted stencil printing technique^[21,24] with mixtures of cPU/ETPTA monomers without any processing solvents, thus permitting the removal of time- and cost-consuming drying steps. The bicontinuous nanophase-separation of the cPU and ETPTA phases as well as the effect of such phase separation on the anion-rectifying behavior and accelerated Li⁺ transport is illustrated (Figure 1b).

The sSIC paste, which includes ETPTA, cPU, and carbonate liquid electrolyte (1 M LiPF₆ in ethylene carbonate (EC, boiling point = 238 °C)/propylene carbonate (PC, boiling point = 242 °C) = 50/50 v/v) was stencil-printed onto a polyethylene terephthalate mold substrate and subsequently solidified after exposure to UV irradiation, yielding a free-standing sSIC film (inset of Figure S2, Supporting Information). The extent of UV-crosslinking of ETPTA was verified by monitoring the change in the Fourier-transform infrared spectroscopy (FT-IR) peaks assigned to the acrylic C=C bonds^[28] of ETPTA (Figure S2, Supporting Information). The characteristic FT-IR peaks of the sSIC appeared to align well with those of pristine ETPTA ($\nu_{\text{O-C-O}}$), cPU ($\nu_{\text{N-H}}$), and liquid electrolyte ($\nu_{\text{O=C-Li}}$, $\nu_{\text{P-F}}$) (Figure 1c). Moreover, energy dispersive X-ray spectroscopy (EDS) mapping images (Figure S3, Supporting Information) demonstrated homogeneous distributions of carbon (C), oxygen (O), nitrogen (N), boron (B), and phosphorous (P), which originate from the ETPTA (acrylates), cPU (pyrrolidinium cations, secondary amines, and tetraphenylborate anions), and liquid electrolyte (hexafluorophosphate anions), respectively. The presence of cPU in the sSIC was further confirmed by using X-ray photoelectron spectroscopy (XPS), specifically the N 1s spectrum (Figure 1d) shows a characteristic peak that is assignable to pyrrolidinium cations.^[29]

The structure of the semi-IPN in the sSIC is a key determinant of ion transport phenomena, the details of which will be investigated below. The nanophase-separated morphology of the sSIC was first characterized. The sSIC film (thickness of ≈ 110 μm) was subjected to solvent etching in acetone. Scanning electron microscopy (SEM) images of the solvent-etched sSIC demonstrate the formation of a nanoporous structure (Figure 1e). FT-IR spectra acquired from the solvent-etched sSIC reveal that the cPU phase and liquid electrolyte were eliminated by the solvent etching, but the UV-crosslinked ETPTA phase remained unaffected (Figure S4, Supporting Information). The solvent etching did not appreciably change the weight of the UV-crosslinked ETPTA, establishing that the ETPTA contained nearly no liquid electrolyte whereas the cPU phase preferentially absorbs liquid electrolyte. These behaviors are attributable to the difference in polarity between the UV-crosslinked ETPTA and cPU. The water contact angles of free-standing sheets of the UV-crosslinked ETPTA and cPU were 83° and 29°, respectively (Figure S5, Supporting Information). Thus, the cPU has a comparably greater polarity that explains for the preferential swelling of the cPU by the electrolyte. The results indicate that the cPU phase in the sSIC supports ion-conducting nanochannels. By comparison, the UV-crosslinked ETPTA

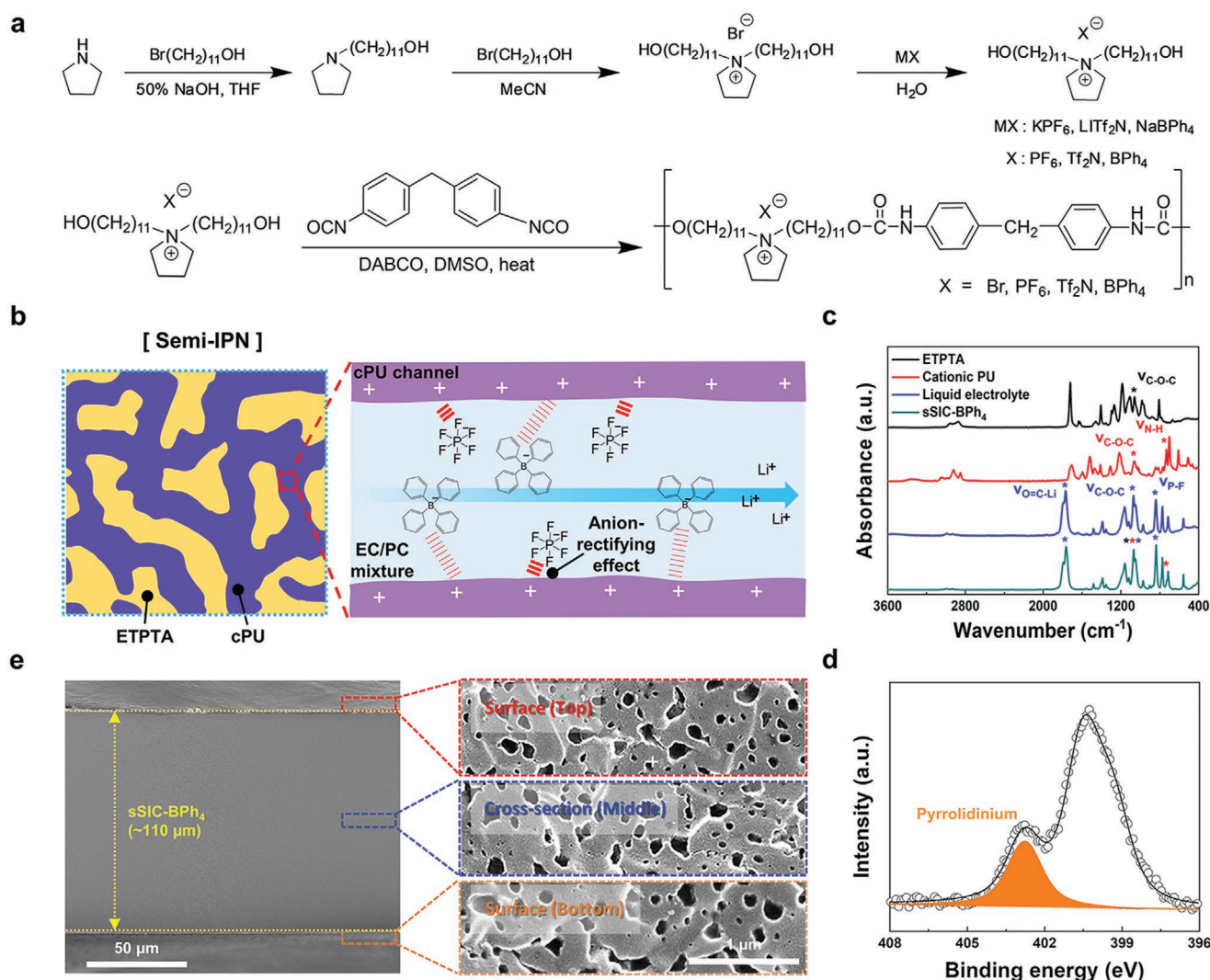


Figure 1. Structural characterizations of the sSIC. a) Synthetic procedure of the cPUs having different counter anions. b) Schematic representation depicting the bicontinuous nanophase-separation of the cPU and ETPTA phases. The advantageous effect of the sSIC on the anion-rectifying effect was conceptually illustrated. c) FT-IR spectra of sSIC-BPh₄ and its components. d) XPS N1s spectrum of the sSIC-BPh₄ showing pyrrolidinium cations. e) Cross-sectional (left) and high-magnification (right) SEM images of the sSIC-BPh₄ after solvent extraction, showing the formation of highly interconnected nanopores throughout the entire cross-section.

phase which was little swollen with the liquid electrolyte serves as a mechanical framework. The nanoporous structure of the solvent-etched sSIC is uniformly distributed at the top, middle, and bottom of the sSIC (right image in Figure 1e), exhibiting the presence of highly interconnected nanopores (i.e., a liquid electrolyte-swollen cPU phase) throughout the cross-section. This nanoporous structure was investigated quantitatively by conducting mercury porosimeter analysis, which established a narrow pore size distribution within the range of 100–1000 nm with an average pore size of 150 nm (Figure S6, Supporting Information). Thus, the cPU and UV-crosslinked ETPTA form a bicontinuous nanophase-separated morphology in the sSIC. Besides this structural analysis, the ion conduction behavior of the sSIC was examined as a function of the cPU/ETPTA composition ratio. Both the ion conductivity and t_{Li^+} increased with cPU content (Figure S7, Supporting Information). sSICs with

a cPU/ETPTA composition ratio of 50/50 w/w exhibited the highest ion conductivity (4.4 mS cm⁻¹) and t_{Li^+} (0.84) at room temperature (RT), indicating its viability as a single Li⁺ conductor. Meanwhile, increasing the cPU content over 50 wt% failed to fabricate free-standing sSIC films (Figure S8, Supporting Information), demonstrating the important role of the UV-crosslinked ETPTA in achieving the structural integrity of the sSIC-BPh₄.

The single-ion conduction behaviors of sSIC were further elucidated by theoretical calculations of the free energy of ion exchange between various monovalent ion pairs (bromide (Br⁻), hexafluorophosphate (PF₆⁻), bis(trifluoromethanesulfonyl) imide (Tf₂N⁻), and tetraphenylborate (BPh₄⁻), different in ionic radii) (Figure S9, Supporting Information). Simulation details are reported in the Experimental Section. Both molecular electrostatic potential and Connolly occupied volume of the counter

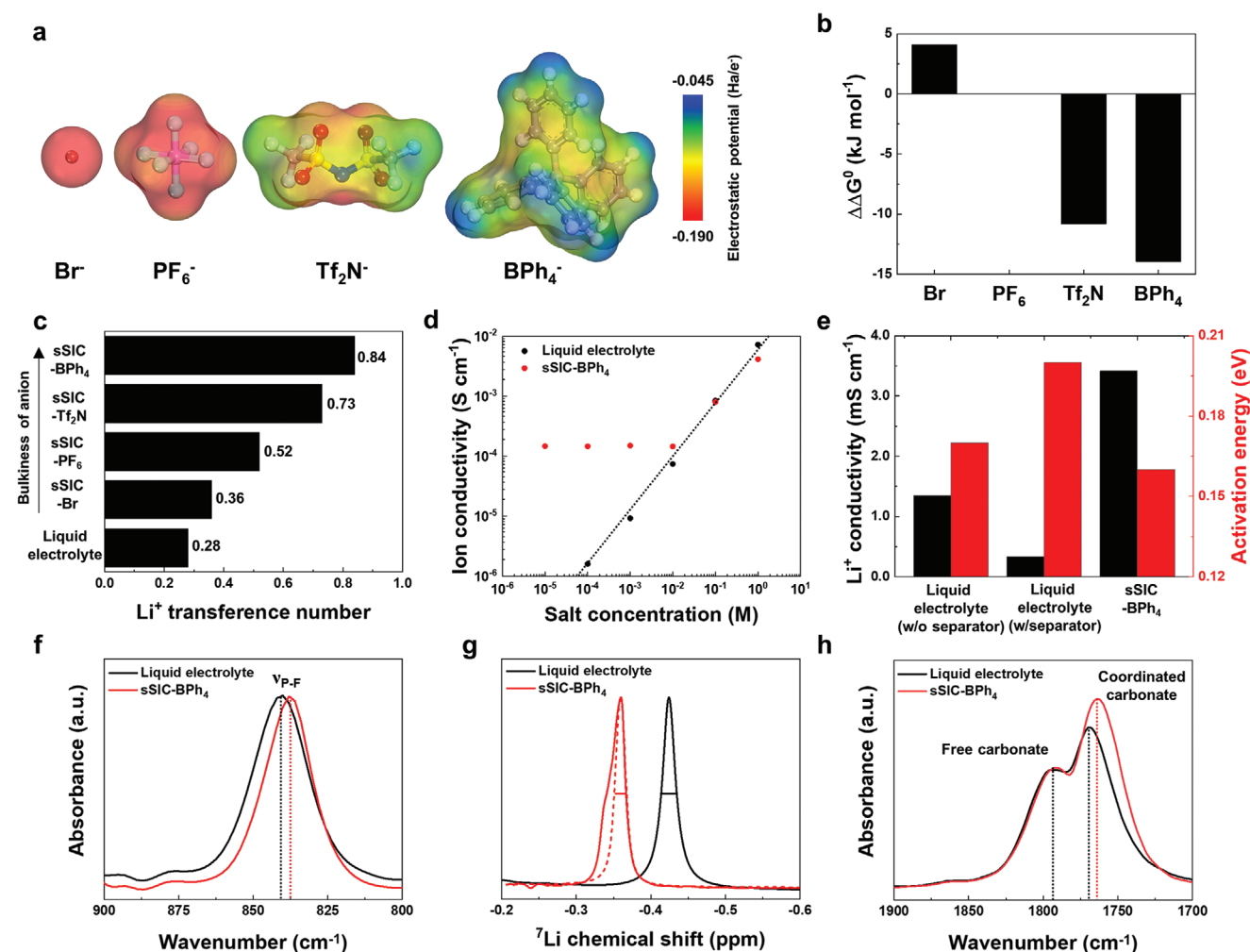


Figure 2. Anion-rectifying behavior of the sSIC. **a**) Counter anions (Br⁻, PF₆⁻, Tf₂N⁻, BPh₄⁻) of the cPU with their electrostatic potential mapping. The red and blue represent the electron-rich and electron-deficient regions, respectively. **b**) Comparison in the free energy of ion exchange between cPU and Li salt (LiPF₆ in the liquid electrolyte) and as a function of counter anions of the cPU. **c**) Li⁺ transference number of the sSIC-BPh₄ as a function of counter anion size of the cPU phase. **d**) Ion conductivity of the sSIC-BPh₄ and liquid electrolyte (1 M LiPF₆ in EC/PC, control sample) as a function of salt concentration. **e**) Li⁺ conductivity at RT and activation energy (E_a) of the sSIC-BPh₄ and liquid electrolyte. To highlight the fast Li⁺ transport of sSIC-BPh₄, Li⁺ conductivity and E_a of liquid electrolyte were compared under the without polyethylene separator membrane condition. **f**) FT-IR spectra (focusing on P-F vibration) of the sSIC-BPh₄ and liquid electrolyte. **g**) ⁷Li NMR spectra of the sSIC-BPh₄ and liquid electrolyte. **h**) FT-IR (focusing on carbonyl stretching vibration) of the sSIC-BPh₄ and liquid electrolyte.

anions are compared (Figure 2a and Figure S10, Supporting Information). The BPh₄⁻ showed the lowest mean value of the electrostatic potential (−0.113 Ha/e⁻) of all the counter anions. Considering that the BPh₄⁻ has the largest occupied volume (352.03 Å³) of all the counter anions, the low electrostatic potential of BPh₄⁻ can be evenly distributed throughout the entire molecule.^[30] As a result, the BPh₄⁻ easily detaches from the cationic groups of the cPU, thereby facilitating ion exchange with PF₆⁻. The free energy of ion exchange between the cPU chains and Li salt of the liquid electrolyte was further determined by calculating the free energy difference between the cPU (i.e., cationic groups (CP) and counter anion (X = Br⁻, PF₆⁻, Tf₂N⁻, and BPh₄⁻) pairs) and the Li salt (i.e., Li–PF₆) by using the following equation: $\Delta\Delta G^\circ = \Delta G^\circ(\text{CP:PF}_6) + \Delta G^\circ(\text{Li:X}) - \Delta G^\circ(\text{CP:X}) - \Delta G^\circ(\text{Li:PF}_6)$. The BPh₄⁻ showed the most negative value for ion

exchange free energy ($\Delta\Delta G^\circ = -13.95$ kJ mol⁻¹) of all counter anions (Figure 2b and Figure S11, Supporting Information), indicating that ion exchange of BPh₄⁻ (from the cPU) with PF₆⁻ (from LiPF₆ in the liquid electrolyte) is thermodynamically favorable.

This unusual single Li⁺ conduction behavior of the sSIC was investigated as a function of the counter anion (Br⁻, PF₆⁻, Tf₂N⁻, and BPh₄⁻) of the cPUs at a fixed cPU/ETPTA composition ratio of 50/50 w/w. In preparing Li electrolytes, salts can be more easily dissociated with larger counter anions.^[31,32] The t_{Li^+} of the sSIC increased with larger counter anions in the cPU (Figure 2c, Figure S12 and Table S1, Supporting Information), revealing that the counter anions influence Li⁺ conduction. The highest t_{Li^+} value (0.84) was observed for the sSIC that contained BPh₄⁻ anions (denoted as sSIC-BPh₄). Meanwhile, the

physical appearance of the free-standing sSIC-BPh₄ was compared with those of a commercial polyethylene (PE) separator (Figure S13, Supporting Information). No difference in the dimensional integrity was observed between the sSIC-BPh₄ and PE separator, regardless of the presence of the carbonate liquid electrolyte.

The ion conductivity of the sSIC-BPh₄ was further examined as a function of the salt concentration of the liquid electrolyte (1 M LiPF₆ in EC/PC = 50/50 v/v) that was predominant in the cPU phase (Figure 2d). As anticipated, the ion conductivity of the sSIC-BPh₄ increased with higher salt concentrations, which appeared similar to the ion conductivity behavior of the liquid electrolyte overall. A notable finding was observed at salt concentrations below 10⁻² M. Below such concentrations, the ion conductivity of the sSIC remained nearly unchanged, while the ion conductivity of the liquid electrolyte was linearly proportional to salt concentration. For example, at a salt concentration of 10⁻⁴ M, the sSIC exhibited an ion conductivity (0.15 mS cm⁻¹) that was approximately two orders of magnitude higher than that of the liquid electrolyte (0.0016 mS cm⁻¹). The unusually high ion conductivity of the sSIC at the dilute salt concentrations can be explained by surface charge-governed nanofluidic transport behaviors, which are observed in ion-exchange membranes.^[33] Specifically, charge screening of nanofluids in the electric double layer can occur near the cPU nanochannel walls, eventually facilitating Li⁺ conduction.

The faster Li⁺ conduction for sSIC-BPh₄ was examined in detail by analyzing the Arrhenius behaviors of Li⁺ conductivity (defined as ion conductivity multiplied by t_{Li^+}) (Figure 2e and Figure S14, Supporting Information). The sSIC-BPh₄ exhibited the highest Li⁺ conductivity at RT and the lowest E_a compared to a liquid electrolyte without or with conventional polyethylene separator membranes (thickness of 20 μm and porosity of 40%). This result demonstrates that the ionic nanochannels in the cPU phase facilitate Li⁺ transport. The single Li⁺ conduction behavior of the sSIC-BPh₄ is underscored by comparisons with the literature (Table S2, Supporting Information). We note that the electrochemical properties of the sSIC was achieved under ambient pressure, whereas the previous studies^[34,35] on inorganic SICs required high operating pressures. Overall, such characteristics demonstrate the viability of sSIC as a practical solid-state electrolyte that is compatible with current battery technologies.

The unusual ion transport phenomena of the sSIC-BPh₄ were further elucidated by using FT-IR analysis. FT-IR spectra acquired from sSIC-BPh₄ showed a characteristic peak at 838 cm⁻¹ that is assignable to the P–F bond vibration, which is shifted to slightly lower wavenumbers than the same peak in liquid electrolytes (840 cm⁻¹) (Figure 2f). As the P–F vibration of PF₆⁻ is influenced by ion association states,^[28,36] this result suggests that PF₆⁻ is electrostatically trapped by positively charged pyrrolidinium moieties that are covalently tethered to the cPU nanochannels. To provide additional information, the local chemical environment of Li⁺ ions in the sSIC-BPh₄ was investigated by using ⁷Li NMR spectroscopy (Figure 2g). An NMR spectrum of the sSIC-BPh₄ showed a singlet ⁷Li peak at -0.36 ppm which was downshifted and narrowed than the singlet ⁷Li peak at -0.42 ppm in the spectrum of liquid electrolyte. This result indicates the sSIC-BPh₄ can facilitate the dissociation of the

Li salts (inferred from the downshifted singlet ⁷Li peak^[37]) and promote the mobility of free Li⁺ ions (inferred from the narrowed singlet ⁷Li peak^[38]) in the sSIC-BPh₄, thereby improving the Li⁺ conductivity.

In addition to the FT-IR and NMR analyses of Li⁺ and PF₆⁻ described above, carbonate solvents were examined by FT-IR spectroscopy to interrogate the carbonyl stretching vibrations that are sensitive to coordination structure.^[37,39] The liquid electrolyte presented two sharp characteristic peaks at 1770 and 1791 cm⁻¹ that are assignable to Li⁺-coordinated and free carbonates, respectively. By comparison, the FT-IR spectrum of the sSIC-BPh₄ showed that the peak associated with Li⁺-coordinated carbonates was downshifted to 1764 cm⁻¹ and had a stronger intensity (Figure 2h). These spectroscopic results demonstrate that the cationic nanochannels of the cPU phase enhance the dissociation of Li salts and also electrostatically capture PF₆⁻ anions, ultimately increasing the concentration of free and mobile Li⁺. The relatively higher conductivity of Li⁺ compared to anions should prevent anion-induced polarization and interfacial side reactions with electrodes, both of which are key problems in conventional liquid electrolytes with low t_{Li^+} values (<0.3). This issue will be discussed in the following section. Meanwhile, we prepared a sSIC-BPh₄ that was swollen with a different liquid electrolyte (0.1 M LiBr in EC/PC = 50/50 v/v). LiBr salt is not typically employed in Li battery electrolytes predominantly because of its poor solubility.^[4] The sSIC-BPh₄ showed much higher Li⁺ conductivity and t_{Li^+} than the LiBr-dissolved liquid electrolyte (Table S3, Supporting Information), which was verified by changes in the ⁷Li NMR spectra (Figure S15, Supporting Information). This underscores the versatility of sSIC-BPh₄ as an effective polymeric medium that can facilitate salt dissociation and enable single-ion conduction.

Anion-induced interfacial side reactions with Li-metal anodes pose a key concern for decaying cycling retention.^[7,8] The high t_{Li^+} of the sSIC appear to be a promising approach to resolve this issue.^[7,8] Li|Li symmetric cells that incorporate the sSIC-BPh₄ and liquid electrolyte (1 M LiPF₆ in EC/PC at 50/50 v/v) were fabricated and their galvanostatic Li plating and stripping cycling behavior was examined at a current density of 1 mA cm⁻² and capacity of 1 mAh cm⁻² (Figure 3a). The control cell (liquid electrolyte) exhibited severe voltage fluctuations with large overpotentials. This indicates that the solid-electrolyte interphase (SEI) layers formed by the interfacial side reaction with liquid electrolyte are not sufficiently stable and thus promote the growth of Li dendrites.^[40] By comparison, the sSIC-BPh₄ cell shows stable cycling performance for over 250 h. The superior Li plating and stripping cyclability of the sSIC-BPh₄ cell was established by analyzing electrochemical impedance spectroscopy (EIS) spectra after cycling tests (Figure 3b). The cell with sSIC-BPh₄ had lower interfacial resistance (145 Ω cm²) than the control cell with the liquid electrolyte (362 Ω cm²), revealing the formation of a stable SEI layer on the Li metal. This result was corroborated by investigating the morphology of the cycled Li metals (Figure 3c). The Li metal assembled with the sSIC-BPh₄ had smooth and dense texture, whereas the Li metal with the liquid electrolyte showed irregular needle-like dendrites.

Structural changes in the cycled Li metal were further elucidated by conducting X-ray photoelectron microscopy (XPS)

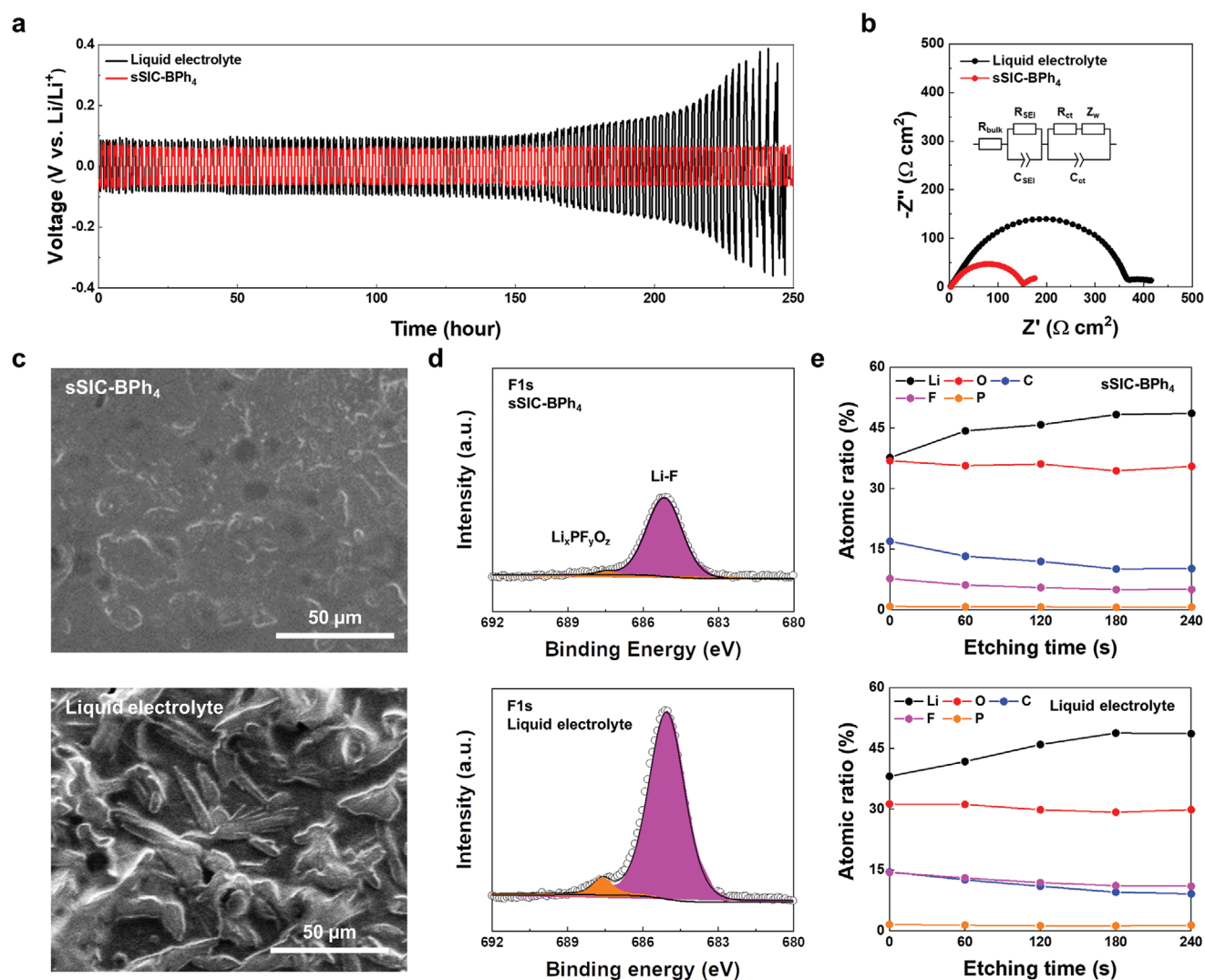


Figure 3. Reduced anion decomposition at the sSIC-Li metal anode interface. a) Voltage profiles of the Li|Li symmetric cells with the sSIC-BPh₄ (vs liquid electrolyte). b) EIS profiles of the Li|Li symmetric cells with the sSIC-BPh₄ (vs liquid electrolyte) after the cycling test (250 h). c) SEM images (surface) of the cycled Li-metal anodes (sSIC-BPh₄ vs liquid electrolyte). XPS analysis of the cycled Li-metal anodes (sSIC-BPh₄ vs liquid electrolyte): d) F1s spectra and e) depth profiles.

analyses. The C1s (Figure S16a, Supporting Information) and O1s spectra (Figure S16b, Supporting Information) showed the presence of typical carbonaceous species (C=C, C-O, C=O, and CO₃²⁻), which form via the decomposition of carbonate-based solvents,^[40] on the top of the Li metals for both the sSIC-BPh₄ and liquid electrolyte cells. This indicates that carbonate solvents act as a charge carrier medium in the sSIC-BPh₄ as well as the liquid electrolyte. Interestingly, the F1s and P2p spectra (Figure 3d and Figure S16c, Supporting Information) of the sSIC-BPh₄ and liquid electrolytes show significant differences. In specific, the cycled Li metal with the sSIC-BPh₄ had weaker characteristic peaks corresponding to LiF (685.1 eV in the F1s spectra) and Li_xPF_yO_z (687.6 and 135.8 eV in the F1s and P2p spectra, respectively) species, which stemmed from the decomposition of LiPF₆, compared to those of the liquid electrolyte. Moreover, XPS depth profiling revealed smaller F content in the cycled Li metal with the sSIC-BPh₄ (Figure 3e),

indicating that the decomposition of PF₆⁻ was suppressed due to the anion-rectifying capabilities of the sSIC-BPh₄. This XPS characterization is consistent with the ion conduction results and ion-pair interactions in the sSIC (shown in Figure 2), underscoring the advantages of the sSIC-BPh₄ as a single Li⁺ conductor in stabilizing the surface of Li metals.

We explored the feasibility of the sSIC as a single-ion conductor for use in Li batteries. It is anticipated that a single-ion conductor will improve the electrochemical reaction kinetics of the battery electrodes and suppress anion-triggered interfacial side reactions at electrodes.^[41,42] The sSIC-BPh₄ was integrated with a NCM811 cathode and Li-metal anode to form a Li-metal cell. A model NCM811 cathode was used to enable focus investigations on the effects of the sSIC-BPh₄. The thickness of the cathode active layer in the model cathode was ≈10 μm that appeared similar to size NCM811 particles, which realizes the electrochemical activities of the NCM811 cathode without the

need to incorporate additional electrolytes into the cathode. A Li metal cell (NCM811 cathode|sSIC-BPh₄|Li-metal anode) exhibited a typical open-circuit voltage of 3.53 V, which was similar to the 3.54 V of a control cell with a liquid electrolyte (1 M LiPF₆ in EC/PC = 50/50 v/v). A cyclic voltammogram (CV) of the cell that included the sSIC-BPh₄ showed electrochemical reversibility in the intercalation and deintercalation of Li⁺ into the NCM811 (Figure 4a). This demonstrates the viability of the sSIC-BPh₄ as an ion conductor in the context of a Li battery. Notably, the difference between the anodic and cathodic peak potentials was smaller than in the control cell. Moreover, galvanostatic intermittent titration technique (GITT) analysis showed that the sSIC-BPh₄ alleviated cell polarization upon repeated current stimuli during charge and discharge reactions (Figure 4b). From the GITT profiles, Li⁺ diffusion coefficients

(D_{Li^+}) of electrode materials were calculated as a function of state of charge (SOC)^[21] (Figure 4c and Table S4, Supporting Information), in which the calculation details are described in the Experimental Section. The cell with the sSIC-BPh₄ showed higher D_{Li^+} values than the control cell with the liquid electrolyte over the whole range of SOC. This result confirms the advantageous effect of the sSIC-BPh₄ on the electrochemical reaction kinetics of electrodes.

The faster electrochemical reaction kinetics enabled by the sSIC-BPh₄ were corroborated by examining the electrochemical behaviors of a Li|Cu asymmetric cell (Figure 4d). The cell that incorporated the sSIC-BPh₄ showed stable Li plating and stripping and a high peak current density, whereas the control cell with the liquid electrolyte exhibited a low peak current density. Moreover, a Tafel plot of the control cell showed a low exchange

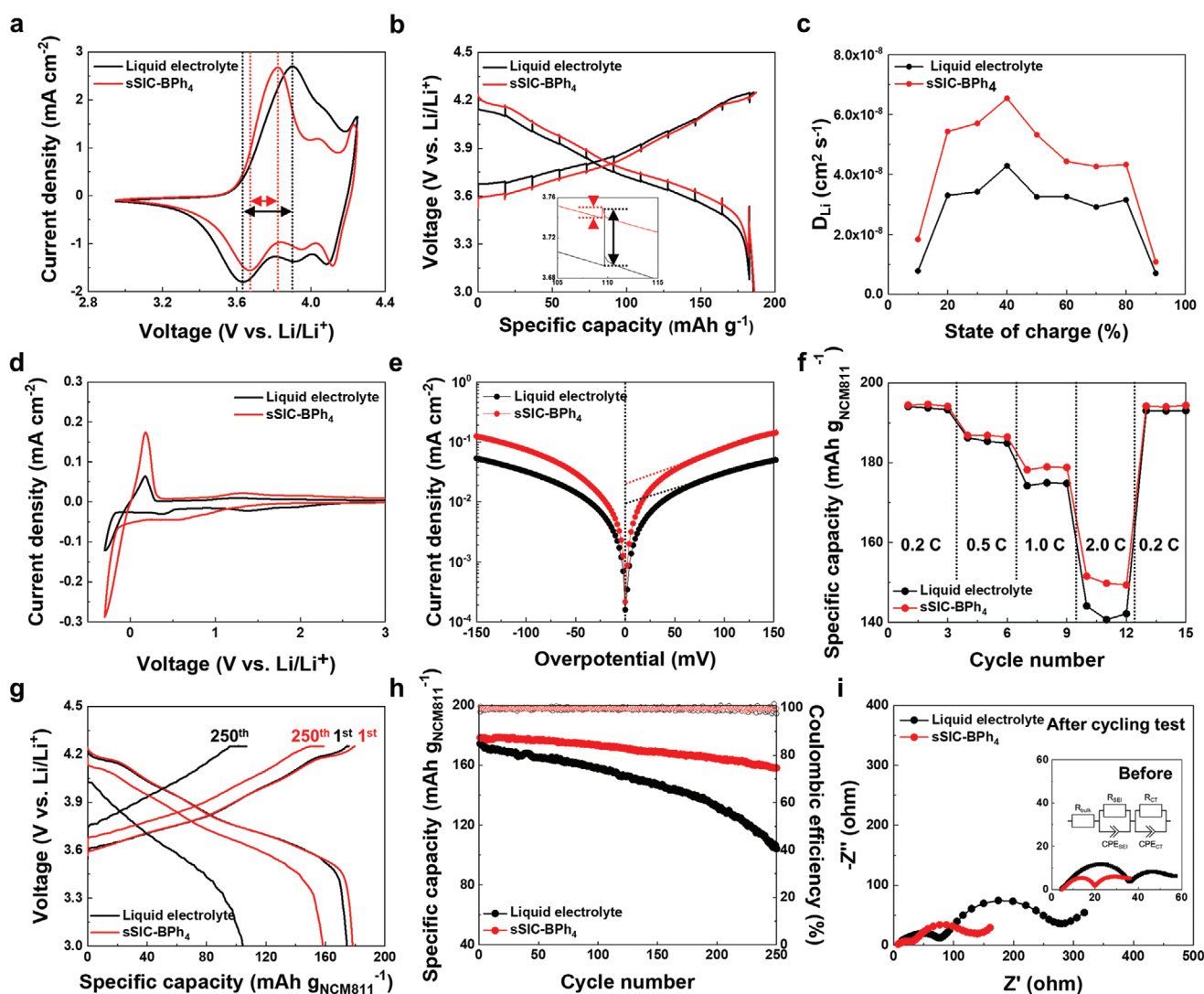


Figure 4. Improved reaction kinetics of the NCM811 cathode and Li metal anode. a) CV and b) GITT profiles of the cell (NCM811 cathode|sSIC-BPh₄|Li-metal anode) containing the sSIC-BPh₄ (vs liquid electrolyte). c) Li⁺ diffusion coefficients as a function of SOC. d) CV profiles and e) Tafel plots of a Li|Cu cell containing the sSIC-BPh₄ (vs liquid electrolyte). f) Rate capability of the cell (NCM811 cathode|sSIC-BPh₄|Li-metal anode), in which the discharge current densities were varied from 0.2 to 2.0 C at a fixed charge current density of 0.2 C. g) Voltage profiles and h) cycling performance of the sSIC-BPh₄ cell (NCM811 cathode|sSIC-BPh₄|Li-metal anode) versus the control cell with liquid electrolyte at a current density of 1.0 C and RT condition. i) EIS profiles of the sSIC-BPh₄ cell after the cycling test. The inset shows the EIS profiles of cell before the cycling test and equivalent circuit model.

current density of 0.010 mA cm^{-2} (Figure 4e), revealing sluggish Li extraction kinetics. By comparison, the cell with the sSIC-BPh₄ had a higher exchange current density of 0.019 mA cm^{-2} . These results demonstrate that the accelerated Li⁺ transport in the sSIC-BPh₄ provides benefits to the reaction kinetics of the NCM811 cathode and Li-metal anode, underscoring the viability of sSIC-BPh₄ as high-performance single Li⁺ conductors for practical applications. The practicality of sSIC-BPh₄ is additionally supported by the fact that sSIC-BPh₄ outperform commercial carbonate liquid electrolytes.

The charge and discharge performances of Li-metal cells with sSIC-BPh₄ were investigated by using a Li-metal cell (NCM811 cathode|sSIC-BPh₄|Li-metal anode). The sSIC-BPh₄ cell exhibited higher discharge capacities than the liquid electrolyte control cell over a wide range of discharge current densities (0.2 to 2.0 C) (Figure 4f). Such faster rate capabilities of the sSIC-BPh₄ cell are consistent with the faster electrochemical reaction kinetics of the electrodes when integrated with sSIC-BPh₄. The cycling performance of the cell was examined at a current density of 1.0 C and RT condition (Figure 4g,h). The sSIC-BPh₄ cell presented a higher capacity retention (=88.6% after 250 cycles) compared to the control cell (59.8%). Such superior cyclability of the sSIC-BPh₄ cell was verified by analyzing the EIS spectra (Figure 4i and Table S5, Supporting Information). The control cell exhibited a large increase in cell impedance (R_{SEI} : 31.4 (before) → 61.7 Ω (after)) and charge transfer (R_{CT} : 19.1 (before) → 204 Ω (after)). By comparison, the sSIC-BPh₄ cell showed markedly lower increases in cell impedance (R_{SEI} : 15.4 (before) → 22.5 Ω (after)) and charge transfer (R_{CT} : 13.6 (before) → 109 Ω (after)). These results demonstrate that the higher Li⁺ conductivity of the sSIC-BPh₄ cell can facilitate charge transfer resistance and alleviate interfacial side reactions with electrodes. Ultimately, these factors improve the cycling performance of the sSIC-BPh₄ cell.

We explored the potential application of sSIC-BPh₄ in anode-free cells. Anode-free cells are a class of post-Li-metal cell because they can support exceptionally high energy densities.^[7,8,14] Yet their poor cycling retention remains a critical challenge in advancing this technology to practical application. An anode-free cell was fabricated by simply using Cu foil as an anode instead of Li metal. The anode-free cell (NCM811 cathode|sSIC-BPh₄|Cu foil) exhibited improved specific capacity compared to the liquid electrolyte control cell (Figure S17, Supporting Information). Moreover, the sSIC-BPh₄ cell showed decent capacity retention with cycling at a current density of 1.0 C and RT condition, whereas the liquid electrolyte control cell suffered a sharp decline in capacity (Figure S18, Supporting Information). Thus, the sSIC-BPh₄ appears to be a viable single-ion conductor that beneficially affects interfacial stability with electrodes and enables accelerated Li⁺ transport. Future work aims to optimize cell design and advance sSIC chemistry to achieve high-energy-density Li-metal cells with robust operating longevity.

3. Conclusion

In summary, we developed the sSIC based on the anion-rectifying semi-IPN with reticulated ion nanochannels. This

quasi-solid-state sSIC was prepared by using processing solvent-free, UV curing-assisted stencil printing that avoided time- and cost-consuming drying steps, exhibiting the manufacturing simplicity and scalability. The resulting sSIC showed bicontinuous nanophase-separation of the liquid electrolyte-swollen cPU, which provided single-ion conducting nanochannels, and UV-crosslinked ETPTA, which contributed to structural integrity. The chemical structure and morphology of the cPU phase were designed to promote surface charge-governed nanofluidic transport and anion-rectifying capability, with specific focus applied to ion-pair (freely movable anions in liquid electrolytes and cations covalently tethered to cPU chains) interaction inside the ion nanochannels. The resulting sSIC-BPh₄ exhibited single-ion conduction behavior and high Li⁺ conductivity (defined as ion conductivity multiplied by t_{Li^+}) even at dilute salt concentrations. This confirmed that the sSIC-BPh₄ exhibited faster Li⁺ transport than commercial carbonate liquid electrolytes. This unique Li⁺ transport phenomena of the sSIC-BPh₄ suppressed anion-triggered interfacial side reactions at the Li-metal anodes and promoted favorable electrochemical reaction kinetics at the electrodes. As a result, the sSIC-BPh₄ improved the rate performance and cycling retention of the Li-metal cell and even enabled the application of sSIC-BPh₄ in anode-free cells. These attributes are far beyond those achievable by carbonate liquid electrolytes. We envision that the sSICs presented herein hold promise as a facile and scalable single-ion conducting quasi-solid-state electrolyte platform, representing a major advance toward practical Li-metal batteries.

4. Experimental Section

Materials: Pyrrolidine (99%), 11-bromo-1-undecanol (97%), anhydrous dimethyl sulfoxide (DMSO) (99.8%), sodium tetraphenylborate (NaBPh₄) (99%), and 1,4-diazabicyclo[2,2,2]octane (DABCO) (>99%) were purchased from Alfa Aesar and used as received. Potassium hexafluorophosphate (KPF₆, >95%), lithium bis(trifluoromethanesulfonyl)imide (LiTf₂N, >98%), and methylene diphenyl 4,4'-diisocyanate (MDI, 97%) were purchased from TCI and used as received. Tetrahydrofuran (THF) and acetonitrile (MeCN) were purchased from SAMCHUN (Korea) and used as received. Ethoxylated trimethylolpropane triacrylate (ETPTA) and 2-hydroxy-2-methylpropiophenone (HMPP) were purchased from Sigma-Aldrich and used as received.

Preparation of Dihydroxyl Pyrrolidinium Monomers: *N*-(11-hydroxyundecyl)pyrrolidine: A mixture solution of pyrrolidine (3.114 g, 43.78 mmol), NaOH 50 wt% solution (4.066 g, 50.82 mmol), 11-bromo-1-undecanol (10.00 g, 39.09 mmol) in THF (50 mL) was refluxed for 24 h. After the reaction mixture was cooled to room temperature, the solvent was removed by a rotoevaporator. The residual mixture was extracted with dichloromethane and water 3 times. The combined organic layer was washed with water and then was dried over anhydrous MgSO₄. Column chromatography through a short silica gel column with THF eluent gave a white solid (7.784 g, 81%). ¹H NMR (500 MHz, CDCl₃, 23°C): δ 1.12 (m, 14H), 1.30 (m, 4H), 1.54 (m, 4H), 2.19 (t, *J* = 8, 2H), 2.26 (s, 4H), 3.30 (t, *J* = 7, 2H). ¹³C NMR (125 MHz, CDCl₃, 23°C): δ 20, 23, 25, 26.4, 26.8, 26.93, 26.96, 26.99, 27, 30.

N,N-di(11-hydroxyundecyl)pyrrolidinium Br⁻: A solution of 11-bromo-1-undecanol (8.910 g, 35.46 mmol) and *N*-(11-hydroxyundecyl)pyrrolidine (7.784 g, 32.24 mmol) in MeCN (45 mL) was refluxed for 24 h. After the reaction completed, the solvent was removed by a rotoevaporator. The residue solid was precipitated by THF 3 times. After the filtration, drying in a vacuum oven gave a white crystalline solid (13.03 g, 82%).

DSC: $T_m = 30\text{ }^{\circ}\text{C}$ (2nd heating) ^1H NMR (500 MHz, DMSO- d_6 , 23 $^{\circ}\text{C}$): δ 1.24 (m, 28H), 1.38 (m, 4H), 1.59 (m, 4H), 2.03 (t, $J = 7$, 4H), 3.19 (m, 4H), 3.35 (m, 4H), 3.45 (t, $J = 5$, 4H), 4.35 (t, $J = 5$, 2H). ^{13}C NMR (125 MHz, DMSO- d_6 , 23 $^{\circ}\text{C}$): δ 21, 22, 25, 26, 28, 29.2, 29.3, 29.4, 29.5, 33, 58, 61, 62. N,N-di(11-hydroxyundecyl)pyrrolidinium PF $_6^-$. The previously obtained bromide salt (2.000 g, 4.060 mmol) was dissolved in deionized water (10 mL) and KPF $_6$ (1.495 g, 8.120 mmol) was added to the solution with vigorous stirring. The produced precipitate was filtered and the filter cake was washed by deionized water 3 times. Drying in a vacuum oven gave a white crystalline solid (2.015 g, 89%). DSC: $T_m = 82\text{ }^{\circ}\text{C}$ (2nd heating). ^1H NMR (500 MHz, acetone- d_6 , 23 $^{\circ}\text{C}$): δ 1.29 (m, 20H), 1.39 (m, 8H), 1.48 (m, 4H), 1.85 (m, 4H), 2.26 (m, 4H), 3.45 (m, $J = 8.5$, 4H), 3.51 (m, 4H), 3.71 (t, $J = 6.5$, 4H). ^{13}C NMR (125 MHz, acetone- d_6 , 23 $^{\circ}\text{C}$): δ 23, 24, 27.7, 27.8, 30, 31.1, 31.2, 31.4, 34, 61, 63.4, 63.5, 64.

N,N-di(11-hydroxyundecyl)pyrrolidinium Tf $_2\text{N}^-$: The previously obtained bromide salt (2.000 g, 4.060 mmol) was dissolved in deionized water (10 mL) and LiTf $_2\text{N}$ (2.331 g, 8.120 mmol) was added with vigorous stirring. After decanting off the upper aqueous layer, the residual viscous liquid was washed with deionized water 3 times. Drying in a vacuum oven gave a yellow viscous liquid (2.128 g, 76%). DSC: $T_g = 51\text{ }^{\circ}\text{C}$ (second heating), no T_m . ^1H NMR (500 MHz, acetone- d_6 , 23 $^{\circ}\text{C}$): δ 1.29 (m, 20H), 1.39 (m, 8H), 1.48 (m, 4H), 1.85 (m, 4H), 2.26 (s, 4H), 3.45 (m, 4H), 3.51 (m, 4H), 3.71 (t, $J = 6.5$, 4H). ^{13}C NMR (125 MHz, acetone- d_6 , 23 $^{\circ}\text{C}$): δ 23, 24, 27.6, 27.9, 30, 31.0, 31.1, 31.3, 34, 61, 63.2, 63.3, 64, 118, 120, 123, 125.

N,N-di(11-hydroxyundecyl)pyrrolidinium BPh $_4^-$: From the previous experiment, the bromide salt (2.000 g, 4.060 mmol) was dissolved in deionized water (10 mL) NaBPh $_4$ (1.667 g, 4.872 mmol) was added with vigorous stirring. The insoluble precipitate was filtered and the filter cake was washed by deionized water three times. Drying in a vacuum oven gave a white solid (2.511 g, 84%). DSC: $T_g = -13\text{ }^{\circ}\text{C}$ (second heating), no T_m . ^1H NMR (500 MHz, acetone- d_6 , 23 $^{\circ}\text{C}$): δ 1.30 (m, 20H), 1.36 (m, 8H), 1.50 (m, 4H), 1.75 (m, 4H), 2.11 (m, 4H), 3.27 (m, 4H), 3.47 (m, 4H), 3.52 (m, 4H), 7.25 (t, $J = 7$, 4H), 7.39 (t, $J = 7.5$, 8H), 7.80 (m, 8H). ^{13}C NMR (125 MHz, acetone- d_6 , 23 $^{\circ}\text{C}$): δ 23, 24, 27., 29.7, 30, 31.0, 31.1, 31.3, 34, 61.121, 125(q, $^2J(\text{B,C}) = 2$), 136, 164(q, $^1J(\text{B,C}) = 50$).

General Synthetic Procedures for the Cationic Polyurathanes (cPUs): A mixture of N,N-di(11-hydroxyundecyl)pyrrolidinium salt (1.000 eq.), MDI (1.000 eq.) and DABCO (130 ppm) as a catalyst in DMSO (20 mL) was stirred for 7 days at 90 $^{\circ}\text{C}$ under N $_2$ atmosphere. Complete consumption of the isocyanate group was demonstrated by FT-IR spectroscopy. After the reaction completion, the mixture was cooled to room temperature, and then the formed polymer was precipitated by methanol (or ethyl acetate). Further purification was followed by a Soxhlet apparatus using MeOH for 12 h. Drying in a vacuum oven at 70 $^{\circ}\text{C}$ led to producing a solid phase cPU.

Fabrication of the sSIC: The sSIC precursor was composed of 1 M LiPF $_6$ in EC:PC = 1:1 v/v without any additives, UV-curable ETPTA (incorporating 5 wt% HMPP as a photoinitiator), and cPU, in which the composition ratio of 1 M LiPF $_6$ in the EC/PC:ETPTA:cPU = 90:5:5 w/w/w. To fabricate the sSIC, the precursor was filled in a home-made polypropylene mold followed by UV irradiation (Hg UV-lamp (Lichtzen) with an irradiation peak intensity of $\approx 2000\text{ mW cm}^{-2}$).

Structural Characterizations: The structural evolution of the SSIC and electrostatic interaction between the positively charged SSIC and free anions were traced by using a Fourier transform infrared spectrometer (FT-IR, Alpha Platinum ATR (Bruker)). The chemical species formed on the cycled Li-metal anodes were investigated by using a X-ray photoelectron spectroscopy (XPS, K-alpha (ThermoFisher)). The surface and cross-sectional morphologies of the SSIC were characterized using a field emission scanning electron microscope (FE-SEM, S-4800 (Hitachi)) in conjunction with an energy-dispersive X-ray spectrometer (EDS). To investigate pore size distribution, the etched SSIC was prepared by solvent extraction (dimethyl carbonate followed by acetone) of the SSIC. The pore size distribution was investigated by using mercury intrusion porosimetry (Auto Pore IV 9520 (Micromeritics)). A penetrometer of 3 mL total volume and 0.4 mL stem volume was loaded with 0.38 g of the etched SSIC. The mercury intrusion volume was obtained in a

pressure range of 0.1–60 000 psia. The pore radius was estimated from the pressure (P) by the Washburn equation:^[43]

$$r_p = \frac{2\gamma \cos\theta}{P} \quad (1)$$

where a contact angle (θ) is 130 $^{\circ}$ and mercury surface tension (γ) is 485 dyn cm $^{-1}$. The chemical shift of Li salts was recorded by using a nuclear magnetic resonance spectroscopy (600 MHz FT-NMR, VNMRS 600 (Agilent)) with 1.6 mm HXY Fast MAS T3 probe. The chemical shift is referenced to a 1 M aqueous LiCl solution at ^7Li (0 ppm). To explore the hydrophilicity of the cPU sheet, 6 μL of water was dropped onto the surface of the samples and contact angles were analyzed using a contact angle analyzer (Attention Theta Flex, Biolin Scientific).

Electrochemical Measurements: The electrochemical performance was investigated using 2032-type coin cell and potentiostat (VSP classic, (Bio-Logic)). A liquid electrolyte (1 M LiPF $_6$ in EC/PC = 1/1 v/v) was used. The ion conductivity was measured with an Li-ion blocking symmetric cell based on an electrochemical impedance spectroscopy (EIS) analysis at a frequency range from 10 $^{-2}$ to 10 6 Hz and an applied amplitude of 10 mV. The Li $^{+}$ transference number ($t_{\text{Li}^{+}}$) was evaluated using a potentiostatic polarization method.^[18] The DC polarization through a Li-ion non-blocking symmetric cell and its sequential EIS before and after the polarization was analyzed to determine the Li $^{+}$ transference number:

$$t_{\text{Li}^{+}} = \frac{I_s(\Delta V - I_0 R_0)}{I_0(\Delta V - I_s R_s)} \quad (2)$$

where ΔV is applied potential, I_0 and R_0 are the initial current and resistance, and I_s and R_s are the steady-state current and resistance after the polarization, respectively. The Li-metal anode cycle test was conducted with the Li|SSIC-BPh $_4$ |Li symmetric cell under a current density of 1 mA cm $^{-2}$ for 1 h per cycle at room temperature. For the cathode test, a LiNi $_{0.8}\text{Co}_{0.1}\text{Mn}_{0.1}\text{O}_2$ (NCM811) cathode was prepared by casting a slurry mixture (NCM811:polyvinylidene fluoride:carbon black = 94:3:3 w/w/w in N-methyl-2-pyrrolidone (NMP)) on an Al foil with cathode thickness of 10 μm . The electrochemical reaction kinetics of the cathode and anode assembled with the sSIC-BPh $_4$ were investigated by cyclic voltammetry (CV). The electrochemical performance of coin-type cells (NCM811|sSIC-BPh $_4$ |Li metal (100 μm) and anode-free cell (NCM811|sSIC-BPh $_4$ |Cu foil) was examined using a cycle tester (PEBC050.1, PNE Solution Co.) in a voltage range of 2.95–4.25 V versus Li/Li $^{+}$. The galvanostatic intermittent titration technique (GITT) analysis was conducted with the cathode half-cell at a current density of 16.7 mA g $^{-1}$ and interruption time between each pulse of 1 h. The Li $^{+}$ diffusion coefficients were calculated using the following equation:^[21]

$$D = \frac{4}{\pi t} \left(\frac{V_m n_m}{S} \right)^2 \left(\frac{\Delta E_s}{\Delta E_t} \right)^2 \quad (3)$$

wherein t and τ represent the duration of current pulse (s) and relaxation time (s); n_m and V_m are the moles of NCM811 and molar volume; S is the electrode-electrolyte interface area (taken as the geometric area of the electrode); ΔE_s and ΔE_t are the steady-state voltage change (V) by the current pulse and overall cell voltage change (V) during the constant current pulse in a single step GITT measurement, respectively.

Simulation Details: Density functional theory (DFT) calculation was performed to determine the free energy of cationic polymer (CP) with counter anions (X) (i.e., Br $^-$, PF $_6^-$, Tf $_2\text{N}^-$, BPh $_4^-$) and Li-salt (i.e., LiPF $_6$) system. All DFT calculations were performed using DMol 3 program^[44,45] with generalized gradient approximation (GGA) and Perdew–Burke–Ernzerhof (PBE) functional.^[46] For the dispersion correction of van der Waals effect, Grimme scheme was used.^[47] In addition, the double numerical basis set with polarization functions (DNP) 4.4 version was used. All electronic relativistic effect was included for the treatment of core electrons. The convergence criterion of the geometry optimization

for energy was set as 1.0×10^{-5} Ha, force was set as 2×10^{-3} Ha \AA^{-1} , and displacement was set as 5×10^{-3} \AA . Additionally, Conductor-like Screening Model (COSMO) method^[48] with dielectric constant (i.e., $\epsilon = 77.36$) of EC/PC was used to consider the solvent environment.^[49,50] The free energies of each state were calculated by the following equation:

$$\Delta G^0 = \Delta H_{\text{corr}} - T\Delta S \quad (4)$$

where ΔH_{corr} includes the interaction and enthalpy changes of each state and ΔS includes the entropy changes of each state.

Supporting Information

Supporting Information is available from the Wiley Online Library or from the author.

Acknowledgements

This work was supported by the Basic Science Research Program (2018M3D1A1058744 and 2021R1A2B5B03001615) through the National Research Foundation of Korea (NRF) grant by the Korean Government (MSIT). This work was also supported by the Technology Innovation Program (20012216 and 20010095) funded by the Ministry of Trade, Industry & Energy (MOTIE, Korea).

Conflict of Interest

The authors declare no conflict of interest.

Author Contributions

S.-K.C., K.-S.O., and J.C.S. contributed equally to this work. S.-K.C. and K.-S.O. designed all electrochemical experiments and analyzed the results. J.S. synthesized the cationic polymer and its semi-IPN structures were analyzed by S.-K.C., K.-S.O., J.C.S., J.E.L., K.M.L., J.C., W.B.L., S.K.K., M.L., and S.-Y.L. J.E.L. and K.M.L. designed and performed all theoretical calculations. S.-K.C., K.-S.O., J.C.S., J.E.L., K.M.L., J.C., W.B.L., S.K.K., M.L., and S.-Y.L. prepared the manuscript. S.K.K., M.L., and S.-Y.L. revised the manuscript critically. All authors have given approval to the final version of the manuscript.

Data Availability Statement

Research data are not shared.

Keywords

accelerated li-ion transport, anion-rectifying capability, polymeric single-ion conductors, reticulated ion nanochannels, semi-interpenetrating polymer network

Received: August 6, 2021

Revised: October 6, 2021

Published online: October 27, 2021

[1] R. Schmich, R. Wagner, G. Höppl, T. Placke, M. Winter, *Nat. Energy* **2018**, *3*, 267.

- [2] T. M. Gür, *Energy Environ. Sci.* **2018**, *11*, 2696.
- [3] J. W. Choi, D. Aurbach, *Nat. Rev. Mater.* **2016**, *1*, 16013.
- [4] K. Xu, *Chem. Rev.* **2004**, *104*, 4303.
- [5] J. Hao, S. Z. F. Yang, H. He, G. Xia, Y. Liu, C. Didier, T. Liu, W. K. Pang, V. K. Peterson, *Proc. Natl. Acad. Sci. USA* **2020**, *117*, 2815.
- [6] J. Liu, Z. Bao, Y. Cui, E. J. Dufek, J. B. Goodenough, P. Khalifah, Q. Li, B. Y. Liaw, P. Liu, A. Manthiram, *Nat. Energy* **2019**, *4*, 180.
- [7] D. Lin, Y. Liu, Y. Cui, *Nat. Nanotechnol.* **2017**, *12*, 194.
- [8] X. B. Cheng, R. Zhang, C. Z. Zhao, Q. Zhang, *Chem. Rev.* **2017**, *117*, 10403.
- [9] Q. Zhao, S. Stalin, C.-Z. Zhao, L. A. Archer, *Nat. Rev. Mater.* **2020**, *5*, 229.
- [10] N. Kamaya, K. Homma, Y. Yamakawa, M. Hirayama, R. Kanno, M. Yonemura, T. Kamiyama, Y. Kato, S. Hama, K. Kawamoto, A. Mitsui, *Nat. Mater.* **2011**, *10*, 682.
- [11] S. Jiao, X. Ren, R. Cao, M. H. Engelhard, Y. Liu, D. Hu, D. Mei, J. Zheng, W. Zhao, Q. Li, N. Liu, B. D. Adams, C. Ma, J. Liu, J.-G. Zhang, W. Xu, *Nat. Energy* **2018**, *3*, 739.
- [12] S. Chen, J. Zheng, L. Yu, X. Ren, M. H. Engelhard, C. Niu, H. Lee, W. Xu, J. Xiao, J. Liu, *Joule* **2018**, *2*, 1548.
- [13] X. Miao, H. Wang, R. Sun, C. Wang, Z. Zhang, Z. Li, L. Yin, *Energy Environ. Sci.* **2020**, *13*, 3780.
- [14] Y.-G. Lee, S. Fujiki, C. Jung, N. Suzuki, N. Yashiro, R. Omoda, D.-S. Ko, T. Shiratsuchi, T. Sugimoto, S. Ryu, J. H. Ku, T. Watanabe, Y. Park, Y. Aihara, D. Im, I. T. Han, *Nat. Energy* **2020**, *5*, 299.
- [15] S. Wang, Y. Zhang, X. Zhang, T. Liu, Y.-H. Lin, Y. Shen, L. Li, C.-W. Nan, *ACS Appl. Mater. Interfaces* **2018**, *10*, 42279.
- [16] Y. Zhang, X. R. Chen, S. Wang, T. Liu, B. Xu, X. Zhang, X. Wang, Y. Shen, Y.-H. Lin, M. Li, L.-Z. Fan, L. Li, C.-W. Nan, *Energy Storage Mater.* **2020**, *25*, 145.
- [17] S. Wang, X. Zhang, S. Liu, C. Xin, C. Xue, F. Richter, L. Li, L. Fan, Y. Lin, Y. Shen, J. Janek, C.-W. Nan, *J. Mater. Chem.* **2020**, *6*, 70.
- [18] M. B. Armand, *Annu. Rev. Mater. Sci.* **1986**, *16*, 245.
- [19] T. Dong, J. Zhang, G. Xu, J. Chai, H. Du, L. Wang, H. Wen, X. Zang, A. Du, Q. Jia, X. Zhou, G. Cui, *Energy Environ. Sci.* **2018**, *11*, 1197.
- [20] J. Zhu, Z. Zhang, S. Zhao, A. S. Westover, I. Belharouak, P.-F. Cao, *Adv. Energy Mater.* **2021**, *11*, 200383.
- [21] K.-S. Oh, J.-H. Kim, S.-H. Kim, D. Oh, S.-P. Han, K. Jung, Z. Wang, L. Shi, Y. Su, T. Yim, S. Yuan, S.-Y. Lee, *Adv. Energy Mater.* **2021**, *11*, 2101813.
- [22] D.-M. Shin, J. E. Bachman, M. K. Taylor, J. Kamcev, J. G. Park, M. E. Ziebel, E. Velasquez, N. N. Jarennattananon, G. K. Sethi, Y. Cui, J. R. Long, *Adv. Mater.* **2020**, *32*, 1905771.
- [23] R. Xu, Y. Xiao, R. Zhang, X.-B. Cheng, C.-Z. Zhao, X.-Q. Zhang, C. Yan, Q. Zhang, J.-Q. Huang, *Adv. Mater.* **2019**, *31*, 1808392.
- [24] X. Guan, Q. Wu, X. Zhang, X. Guo, C. Li, J. Xu, *Chem. Eng. J.* **2020**, *382*, 122935.
- [25] H. Yuan, J. Luan, Z. Yang, J. Zhang, Y. Wu, Z. Lu, H. Liu, *ACS Appl. Mater. Interfaces* **2020**, *12*, 7249.
- [26] K. Liu, S. Jiang, T. Dzwiniel, H. Kim, Z. Yu, N. L. Dietz Rago, J. J. Kim, T. T. Fister, J. Yang, Q. Liu, J. Gillbert, L. Cheng, V. Srinivasan, Z. Zhang, C. Liao, *ACS Appl. Mater. Interfaces* **2020**, *12*, 29162.
- [27] K. Jeong, S. Park, S.-Y. Lee, *J. Mater. Chem. A* **2019**, *7*, 1917.
- [28] S. K. Cho, H. I. Kim, J. W. An, K. Jung, H. Bae, J. H. Kim, T. Yim, S. Y. Lee, *Adv. Funct. Mater.* **2020**, *30*, 2070157.
- [29] V. Lockett, R. Sedev, S. Harmer, J. Ralston, M. Horne, T. Rodopoulos, *Phys. Chem. Chem. Phys.* **2010**, *12*, 13816.
- [30] A. Boisset, L. Athouël, J. Jacquemin, P. Porion, T. Brousse, M. Anouti, *J. Phys. Chem. C* **2013**, *117*, 7408.
- [31] M. Lee, Y. K. Kwon, J. Kim, U. H. Choi, *Macromolecules* **2019**, *52*, 2314.
- [32] M. Lee, U. H. Choi, R. H. Colby, H. W. Gibson, *Chem. Mater.* **2010**, *22*, 5814.

- [33] T. Li, S. X. Li, W. Kong, C. Chen, E. Hitz, C. Jia, J. Dai, X. Zhang, R. Briber, Z. Siwy, *Sci. Adv.* **2019**, 5, eaau4238.
- [34] S. Wang, M. Tang, Q. Zhang, B. Li, S. Ohno, F. Walther, R. Pan, X. Xu, C. Xin, W. Zhang, L. Li, Y. Shen, F. H. Richter, J. Janek, C.-W. Nan, *Adv. Energy Mater.* **2021**, 11, 2101370.
- [35] S. Wang, W. Zhang, X. Chen, D. Das, R. Ruess, A. Gautam, F. Walther, S. Ohno, R. Koerver, Q. Zhang, W. G. Zeier, F. H. Richter, C.-W. Nan, J. Janek, *Adv. Energy Mater.* **2021**, 11, 2100654.
- [36] G. Li, Z. Liu, D. Wang, X. He, S. Liu, Y. Gao, A. AlZahrani, S. H. Kim, L. Q. Chen, D. Wang, *Adv. Energy Mater.* **2019**, 9, 1900704.
- [37] H. Chen, H. Tu, C. Hu, Y. Liu, D. Dong, Y. Sun, Y. Dai, S. Wang, H. Qian, Z. Lin, L. Chen, *J. Am. Chem. Soc.* **2018**, 140, 896.
- [38] D. A. Vazquez-Molina, G. S. Mohammad-Pour, C. Lee, M. W. Logan, X. Duan, J. K. Harper, F. J. Uribe-Romo, *J. Am. Chem. Soc.* **2016**, 138, 9767.
- [39] M. Nie, D. P. Abraham, D. M. Seo, Y. Chen, A. Bose, B. L. Lucht, *J. Phys. Chem. C* **2013**, 117, 25381.
- [40] D. Lv, Y. Shao, T. Lozano, W. D. Bennett, G. L. Graff, B. Polzin, J. Zhang, M. H. Engelhard, N. T. Saenz, W. A. Henderson, *Adv. Energy Mater.* **2015**, 5, 1402290.
- [41] T. F. Fuller, M. Doyle, J. Newman, *J. Electrochem. Soc.* **1994**, 141, 1.
- [42] M. Doyle, T. F. Fuller, J. Newman, *J. Electrochem. Soc.* **1993**, 140, 1526.
- [43] R. Pavlicek, S. C. Barton, N. Leonard, H. Romero, S. McKinney, G. McCool, A. Serov, D. Abbott, P. Atanassov, S. Mukerjee, *J. Electrochem. Soc.* **2018**, 165, F589.
- [44] B. Delley, *J. Chem. Phys.* **1990**, 92, 508.
- [45] B. Delley, *J. Chem. Phys.* **2000**, 113, 7756.
- [46] J. P. Perdew, K. Burke, M. Ernzerhof, *Phys. Rev. Lett.* **1996**, 77, 3865.
- [47] A. Allouche, *J. Comput. Chem.* **2012**, 32, 174.
- [48] A. Klamt, G. Schüürmann, *J. Chem. Soc., Perkin Trans. 2* **1993**, 2, 799.
- [49] H. Looyenga, *Mol. Phys.* **1965**, 9, 501.
- [50] J. Y. Song, Y. Y. Wang, C. C. Wan, *J. Electrochem. Soc.* **2000**, 147, 3219.